

# Performance of wall-modeled LES for external aerodynamics in the NASA Juncture Flow

By A. Lozano-Durán, S. T. Bose AND P. Moin

## 1. Motivation and objectives

The use of computational fluid dynamics (CFD) for external aerodynamic applications has been a key tool for aircraft design in the modern aerospace industry. CFD methodologies with increasing functionality and performance have greatly improved our understanding and predictive capabilities of complex flows. These improvements suggest that Certification by Analysis (CbA) –prediction of the aerodynamic quantities of interest by numerical simulations (Clark *et al.* 2020) may soon be a reality. CbA is expected to narrow the number of wind tunnel experiments, reducing both the turnover time and cost of the design cycle. However, flow predictions from the state-of-the-art CFD solvers are still unable to comply with the stringent accuracy requirements and computational efficiency demanded by the industry. These limitations are imposed, largely, by the defiant ubiquity of turbulence. In the present work, we investigate the performance of wall-modeled large-eddy simulation (WMLES) to predict the mean flow quantities over the fuselage and wing-body junction of the NASA Juncture Flow Experiment (Rumsey *et al.* 2019).

Computations submitted to previous AIAA Drag Prediction Workshops (Vassberg *et al.* 2008) have displayed large variations in the prediction of separation, skin friction, and pressure in the corner-flow region near the wing trailing edge. To improve the performance of CFD, NASA has developed a validation experiment for a generic full-span wing-fuselage junction model at subsonic conditions. The reader is referred to Rumsey *et al.* (2019) for a summary of the history and goals of the NASA Juncture Flow Experiment (see also Rumsey & Morrison 2016; Rumsey *et al.* 2016). The geometry and flow conditions are designed to yield flow separation in the trailing edge corner of the wing, with recirculation bubbles varying in size with the angle of attack (AoA). The model is a full-span wing-fuselage body that was configured with truncated DLR-F6 wings, both with and without leading-edge horn at the wing root. The model has been tested at a chord Reynolds number of 2.4 million, and AoA ranging from -10 degrees to +10 degrees in the Langley 14- by 22-foot Subsonic Tunnel. An overview of the experimental measurements can be found in Kegerise *et al.* (2019). The main aspects of the planning and execution of the project are discussed by Rumsey (2018), along with details about the CFD and experimental teams.

To date, most CFD efforts on the NASA Juncture Flow Experiment have been conducted using RANS or hybrid-RANS solvers. Lee *et al.* (2017) performed the first CFD analysis to aid the NASA Juncture Flow committee in selecting the wing configuration for the final experiment. Lee *et al.* (2018) presented a preliminary CFD study of the near wing-body juncture region to evaluate the best practices in simulating wind tunnel effects. Rumsey *et al.* (2019) used FUN3D to investigate the ability of RANS-based CFD

solvers to predict the flow details leading up to separation. The study comprised different RANS turbulence models such as a linear eddy viscosity one-equation model, a nonlinear version of the same model, and a full second-moment seven-equation model. Rumsey *et al.* (2019) also performed a grid sensitivity analysis and CFD uncertainty quantification. Comparisons between CFD simulations and the wind tunnel experimental results have been recently documented by Lee & Pulliam (2019).

NASA has recognized WMLES as a critical pacing item for “developing a visionary CFD capability required by the notional year 2030”. According to NASA’s recent CFD Vision 2030 report (Slotnick *et al.* 2014), hybrid RANS/LES (Spalart *et al.* 1997; Spalart 2009) and WMLES (Bose & Park 2018) are identified as the most viable approaches for predicting realistic flows at high Reynolds numbers in external aerodynamics. However, WMLES has been less thoroughly investigated. In the present study, we perform WMLES of the NASA Juncture Flow. Other attempts of WMLES of the same flow configuration include the works by Iyer & Malik (2020), Ghate *et al.* (2020), and Lozano-Durán *et al.* (2020). These authors highlighted the capabilities of WMLES for predicting wall pressure, velocity and Reynolds stresses, especially compared with RANS-based methodologies. Nonetheless, it was noted that WMLES is still far from providing the robustness and stringent accuracy required for CbA, especially in the separated regions and wing-fuselage corners. The goal of this brief is to systematically quantify some of these errors. Modeling improvements to alleviate these limitations are discussed in the companion brief by Lozano-Durán & Bae (2020), which can be found in this volume.

This brief is organized as follows. The flow setup, mathematical modeling, and numerical approach are presented in Section 2. The strategies for grid generation are discussed in Section 3. The results are presented in Section 4, which includes the prediction and error scaling of the mean velocity profiles and Reynolds stresses for three different locations on the aircraft: the upstream region of the fuselage, the wing-body juncture, and the wing-body juncture close to the trailing edge. Finally, conclusions are offered in Section 5.

## 2. Numerical Methods

### 2.1. Flow conditions and computational setup

We use the NASA Juncture Flow geometry with a wing based on the DLR-F6 and a leading-edge horn to mitigate the effect of the horseshoe vortex over the wing-fuselage juncture. The model wingspan is nominally 3397.2 mm, the fuselage length is 4839.2 mm, and the crank chord (chord length at the Yehudi break) is  $L = 557.1$  mm. The frame of reference is such that the fuselage nose is located at  $x = 0$ , the  $x$ -axis is aligned with the fuselage centerline, the  $y$ -axis denotes spanwise direction, and the  $z$ -axis is the vertical direction. The associated instantaneous velocities are denoted by  $u$ ,  $v$ , and  $w$ , and occasionally by  $u_1$ ,  $u_2$ , and  $u_3$ .

In the experiment, the model was tripped near the front of the fuselage and on the upper and lower surfaces of both wings. In our case, preliminary calculations showed that tripping was also necessary to trigger the transition to turbulence over the wing. Hence, the geometry of the wing was modified by displacing in the  $z$  direction a line of surface mesh points close to the leading edge by 1 mm along the suction side of the wing, and by -1 mm along the pressure side. The tripping lines follow approximately the location of the tripping dots used in the experimental setup for the left wing (lower surface  $x = (4144 - y)/2.082$ ; upper surface  $x = (3775 - y)/1.975$  for  $y < -362$  and

$x = (2847 - y)/1.532$  for  $y > -362$ ). Tripping using dots mimicking the experimental setup was also tested. It was found that the results over the wing-body juncture show little sensitivity to the tripping due to the presence of the incoming boundary layer from the fuselage. No tripping was needed on the fuselage, which naturally transitioned from laminar to turbulence.

In the wind tunnel, the model was mounted on a sting aligned with the fuselage axis. The sting was attached to a mast that emerged from the wind tunnel floor. Here, all calculations are performed in free air conditions, and the sting and mast are ignored. The computational setup is such that the dimensions of the domain are about five times the length of the fuselage in the three directions. The Reynolds number is  $Re = LU_\infty/\nu = 2.4$  million based on the crank chord length  $L$ , and freestream velocity  $U_\infty$ . The freestream Mach number is  $Ma = 0.189$ , the freestream temperature is  $T = 288.84$  K, and the dynamic pressure is 2476 Pa. We impose a uniform plug flow as the inflow boundary condition. The Navier–Stokes characteristic boundary condition for subsonic non-reflecting outflow is imposed at the lateral boundaries, outflow and top boundaries (Poinsot & Lele 1992). At the walls, we impose Neumann boundary conditions with the shear stress provided by the wall model as described in Section 2.2.

## 2.2. Subgrid-scale and wall modeling

The simulations are conducted with the high-fidelity solver charLES developed by Cascade Technologies, Inc. The code integrates the compressible LES equations using a kinetic-energy conserving, second-order accurate, finite volume method. The numerical discretization relies on a flux formulation which is approximately entropy preserving in the inviscid limit, thereby limiting the amount of numerical dissipation added into the calculation. The time integration is performed with a third-order Runge-Kutta explicit method. The SGS model is the dynamic Smagorinsky model (Germano *et al.* 1991) with the modification by Lilly (1992).

We utilize a wall model to overcome the restrictive grid-resolution requirements to resolve the small-scale flow motions in the vicinity of the walls. The no-slip boundary condition at the walls is replaced by a wall-stress boundary condition. The wall stress is obtained from the wall model and the walls are assumed isothermal. We use an algebraic equilibrium wall model derived from the integration of the one-dimensional equilibrium stress model along the wall-normal direction (Wang & Moin 2002; Kawai & Larsson 2012; Larsson *et al.* 2016). The matching location for the wall model is the first off-wall cell center of the LES grid. No temporal filtering or treatments were used.

## 3. Grid strategies and cost

### 3.1. Grid generation: constant-size grid vs. boundary-layer-conforming grid

The mesh generation is based on a Voronoi hexagonal close-packed point-seeding method. We follow two strategies for grid generation:

(i) Constant-size grid. In the first approach, we set the grid size in the vicinity of the aircraft surface to be roughly isotropic  $\Delta \approx \Delta_x \approx \Delta_y \approx \Delta_z$ . The number of layers in the direction normal to the wall of size  $\Delta$  is also specified. We set the far-field grid resolution,  $\Delta_{\text{far}} > \Delta$ , and create additional layers with increasing grid size to blend the near-wall grid with the far-field size. The meshes are constructed using a Voronoi diagram and ten iterations of Lloyd’s algorithm to smooth the transition between layers with different grid resolutions. Figure 1(a) illustrates the grid structure for  $\Delta = 2$  mm

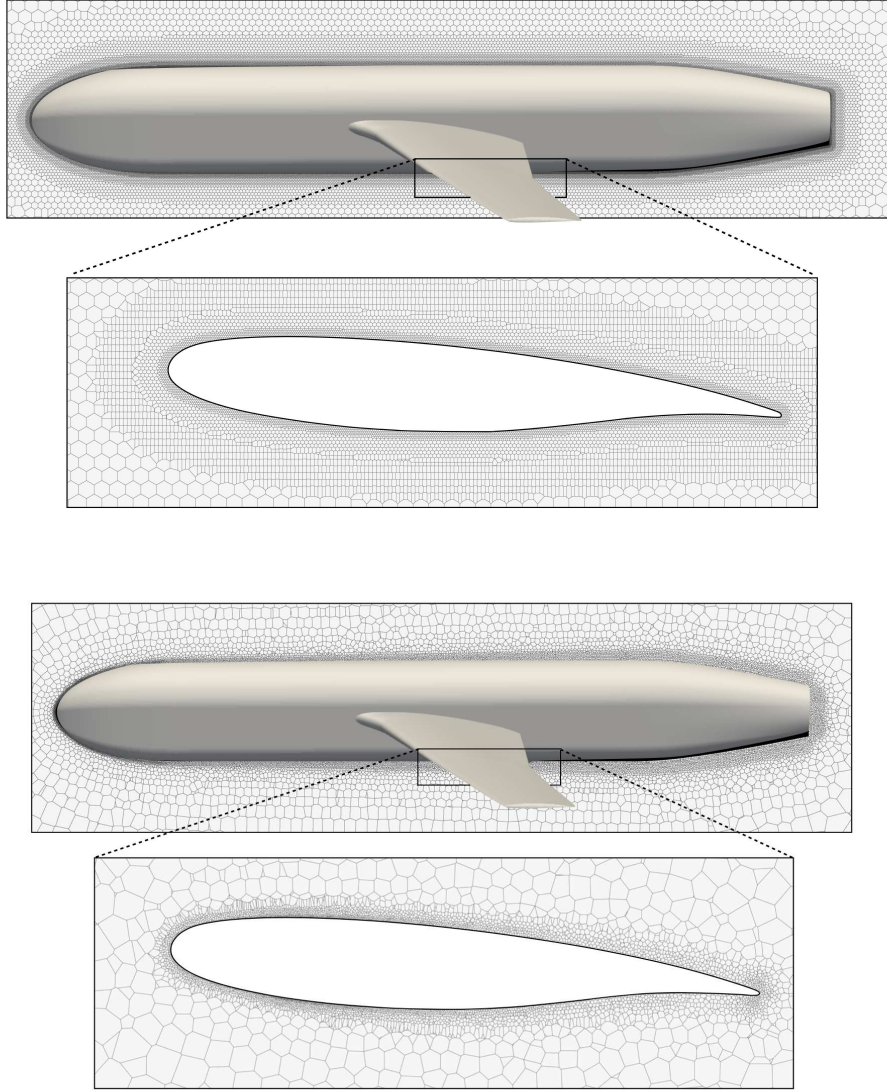


FIGURE 1. Visualization of Voronoi control volumes for (top) constant-size grid following strategy i) with  $\Delta = 2$  mm and  $\Delta_{\text{far}} = 80$  mm and (bottom) boundary-layer-conforming grid following strategy ii) with  $N_{bl} = 5$  and  $Re_{\Delta}^{\text{min}} = 8 \times 10^3$ .

and  $\Delta_{\text{far}} = 80$  mm. This grid-generation approach is algorithmically simple and efficient. However, it is agnostic to details of the actual flow such as wake/shear regions and boundary-layer growth. This implies that flow regions close to the fuselage nose and wing leading edge are underresolved (less than one point per boundary-layer thickness), whereas the wing trailing edge and the downstream-fuselage regions are seeded with up to hundreds of points per boundary-layer thickness. The gridding strategy (ii) aims at alleviating this issue.

(ii) Boundary-layer-conforming grid. In the second gridding strategy, we account for the actual growth of the turbulent boundary layers  $\delta$  by seeding the control volumes consistently. We refer to this approach as boundary-layer-conforming grid (BL-conforming grid). The method necessitates two parameters. The first one is the number of points per boundary-layer thickness,  $N_{bl}$ , such that  $\Delta_x \approx \Delta_y \approx \Delta_z \approx \Delta \approx \delta/N_{bl}$ , which is a function of space. The second parameter is less often discussed in the literature and is the minimum local Reynolds number that we are willing to represent in the flow,  $Re_{\Delta}^{\min} \equiv \Delta_{\min} U_{\infty} / \nu$ , where  $\Delta_{\min}$  is the smallest grid resolution allowed. This is a necessary constraint as  $\delta \rightarrow 0$  at the body leading edge, which would impose a large burden on the number of points required. The last condition is a geometric constraint such that  $\Delta$  is smaller than the local radius of curvature  $R$  of the surface. The grid is then constructed by seeding points within the boundary layer with space-varying grid size

$$\Delta(x, y, z) \approx \min \left[ \max \left( \frac{\gamma \delta}{N_{tbl}}, \frac{Re_{\Delta}^{\min} \nu}{U_{\infty}} \right), \beta R \right], \quad (3.1)$$

where  $\gamma = 1.2$  is a correction factor for  $\delta$  to ensure the near-wall grid contains the instantaneous boundary layer, and  $\beta = 1/2$ . Note that the grid is still locally isotropic and the characteristic size of the control volumes is  $\delta/N_{tbl}$  in the three spatial directions. Figure 1(b) shows the structure of a BL-conforming grid with  $N_{bl} = 5$  and  $Re_{\Delta}^{\min} = 8 \times 10^3$ . Additional control volumes of increasing size are created to blend the near-wall grid with the far-field grid of size  $\Delta_{\text{far}}$ .

The gridding approach above requires an estimation of the boundary-layer thickness at each location of the aircraft surface. The method proposed here is based on measuring the deviation of the viscous flow solution from the reference inviscid flow. This is achieved by conducting two simulations: one WMLES, whose velocity is denoted as  $\mathbf{u}$ , and one inviscid simulation (no SGS model and free-slip at the wall), with velocity denoted by  $\mathbf{u}_I$ . The grid generation of both simulations follows strategy (i) with  $\Delta = 2$  mm. Boundary layers at the leading edge with thickness below 2 mm are estimated by extrapolating the solution using a power law. Two examples of mean velocity profiles for  $\mathbf{u}$  and  $\mathbf{u}_I$  are shown in Figures 2(a) and (b). The three-dimensional surface representing the boundary layer edge  $S_{tbl}$  is identified as the loci of

$$S_{tbl} \equiv \left\{ (x, y, z) : \frac{\| \langle \mathbf{u}_I(x, y, z) \rangle - \langle \mathbf{u}(x, y, z) \rangle \|}{\| \langle \mathbf{u}_I(x, y, z) \rangle \|} = 0.01 \right\}, \quad (3.2)$$

where  $\langle \cdot \rangle$  denotes time-average. Finally, at each point of the aircraft surface  $(x_a, y_a, z_a)$ , the boundary-layer thickness  $\delta$  is defined as the minimum spherical distance between  $\mathbf{x}_a = (x_a, y_a, z_a)$  and  $\mathbf{x} = (x, y, z) \in S_{tbl}$ ,

$$\delta(\mathbf{x}_a) \equiv \|\mathbf{x}_a - \mathbf{x}\|_{\min}, \quad \forall \mathbf{x} \in S_{tbl}. \quad (3.3)$$

The boundary-layer thickness for the flow conditions of the NASA Juncture Flow is shown in Figure 2(c) and ranges from 0 mm at the leading edge of the wing to  $\sim 30$  mm at the trailing edge of the wing. Thicker boundary layers about 50 mm are found in the downstream region of the fuselage. Equation (3.2) might be interpreted as the definition for a turbulent/nonturbulent interface, although it also applies to laminar regions. Other approaches for defining  $S_{tbl}$  were also explored and combined with Eq. (3.3), such as isosurfaces of Q-criterion. Nonetheless, the present flow case is dominated by attached boundary layers and Eq. (3.2) yields reasonable results for the purpose of generating a BL-conforming grid.

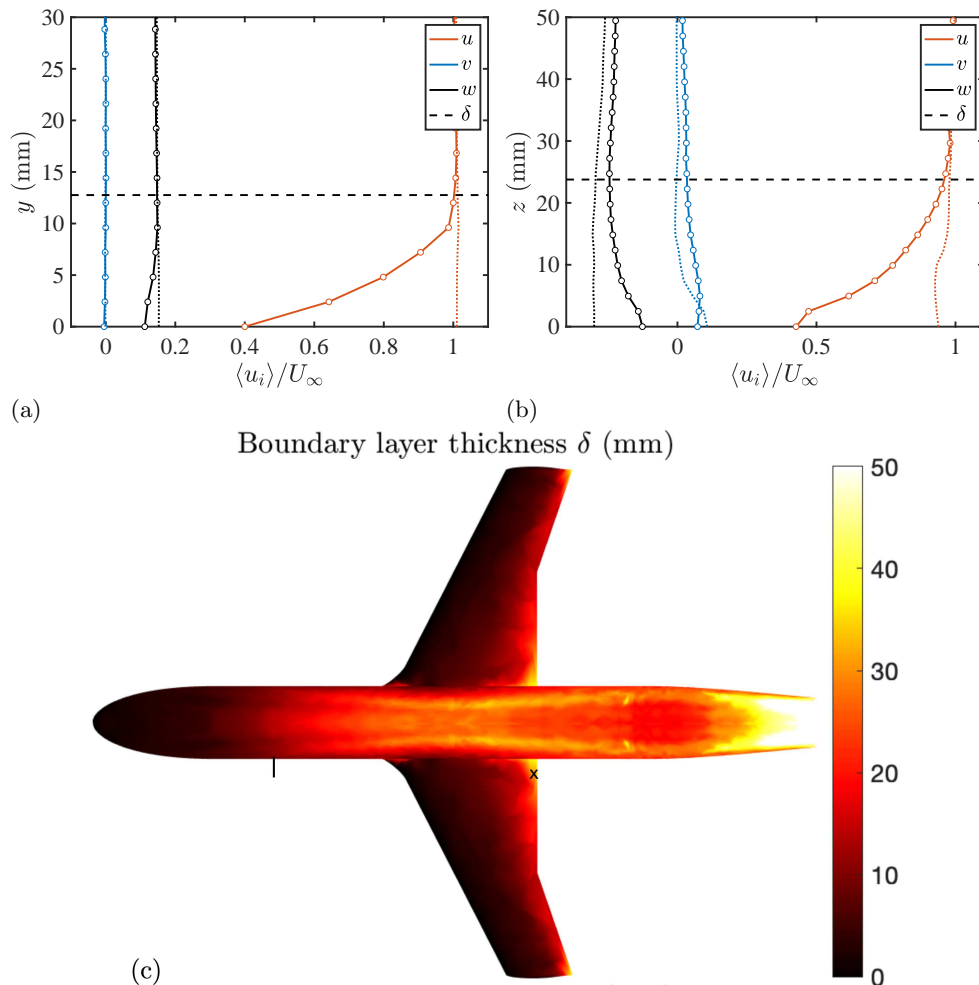


FIGURE 2. The three mean velocity components for  $\langle \mathbf{u} \rangle$  (lines with symbols) and  $\langle \mathbf{u}_I \rangle$  (dotted lines), and boundary layer height (dashed). The locations of the mean profiles are indicated in panel (c) by the solid line for panel (a) and the cross for panel (b). (c) Boundary-layer thickness (in millimeters) for the NASA Juncture Flow at AoA = 5 degrees and  $Re = 2.4 \times 10^6$ .

### 3.2. Number of grid points

We estimate the number of grid points (or control volumes) to conduct WMLES of the NASA Juncture Flow as a function of the number of points per boundary-layer thickness ( $N_{bl}$ ) and the minimum grid Reynolds number ( $Re_{\Delta}^{\min}$ ). We assume the gridding strategy (ii) and utilize the Juncture Flow geometry. The boundary-layer thickness was obtained following the procedure in Section 3.1. The total number of points,  $N_{\text{points}}$ , to grid the boundary layer spanning the surface area of the aircraft  $S_a$  is

$$N_{\text{points}} = \int_0^\delta \int_{S_a} \frac{1}{\Delta(x_{\parallel}, y_{\parallel})^3} dx_{\parallel} dy_{\parallel} dn = \int_{S_a} \frac{N_{bl}}{\Delta(x_{\parallel}, y_{\parallel})^2} dx_{\parallel} dy_{\parallel}, \quad (3.4)$$

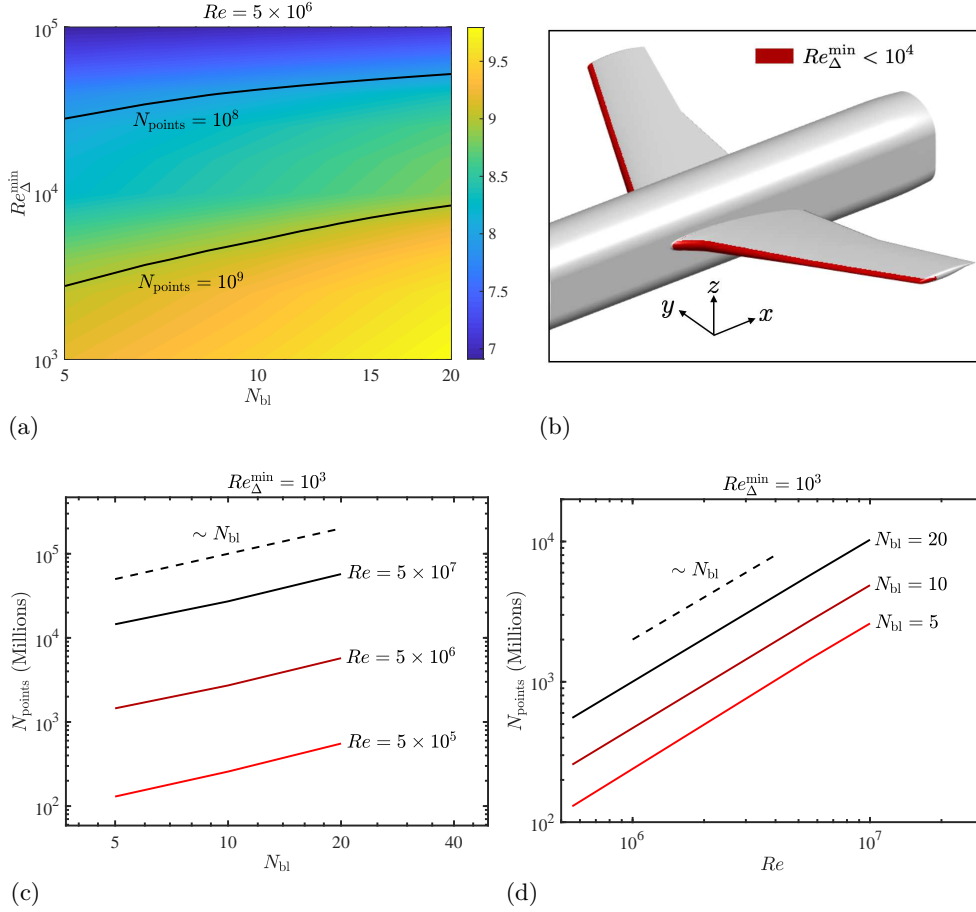


FIGURE 3. (a) Logarithm of the number of points ( $\log_{10} N_{\text{points}}$ ) required for WMLES of the NASA Juncture Flow geometry as a function of the number of grid points per boundary-layer thickness ( $N_{bl}$ ) and minimum grid Reynolds number ( $Re_{\Delta}^{\min}$ ) for  $Re = 5 \times 10^6$ . (b) Subgrid boundary-layer region (in red) for  $Re_{\Delta}^{\min} = 10^4$  at  $Re = 5 \times 10^6$ . Panels (c) and (d) are the number of grid points as a function of (c)  $N_{bl}$  and (d)  $Re$ .

where  $x_{\parallel}$ ,  $y_{\parallel}$  are the aircraft wall-parallel directions, and  $n$  is the wall-normal direction (see also Chapman 1979; Spalart *et al.* 1997; Choi & Moin 2012). Equation (3.4) is integrated numerically and the results are shown in Figure 3. The cost map in Figure 3(a) contains  $\log_{10}(N_{\text{points}})$  as a function of  $N_{bl}$  and  $Re_{\Delta}^{\min}$ . The accuracy of the solution is expected to improve for increasing values of  $N_{bl}$ , i.e., higher energy content resolved by the LES grid, and decrease with increasing  $Re_{\Delta}^{\min}$ . The latter sets the minimum boundary-layer thickness that can be resolved by the LES grid (i.e., the largest thickness of the subgrid boundary layer). Figure 3(b) provides a visual illustration of the subgrid-boundary-layer region for  $Re_{\Delta}^{\min} < 10^4$ , which is confined to a small region (less than 10% of the chord) at the leading edge of the wing.

The Reynolds number considered in Figure 3(a) is  $Re = 5 \times 10^6$ , which is representative of wind tunnel experiments. A Reynolds number typical of aircraft in flight conditions is  $Re \approx 5 \times 10^7$ , which would increase  $N_{\text{points}}$  by a factor of ten due to the thinning of the

boundary layers. More precisely, the increase in  $N_{\text{points}}$  is proportional to  $Re$  and  $N_{bl}$ , and roughly inversely proportional to  $Re_{\Delta}^{\text{min}}$ . The scaling properties of Eq. (3.4) can be explained by assuming that the boundary layer over the aircraft is fully turbulent and grows as  $\delta \sim (x-x_e)[(x-x_e)U_{\infty}/\nu]^{-m}$ , where  $x_e$  is the streamwise distance to the closest leading edge and  $m \approx -1/7$  for a zero-pressure gradient flat-plate turbulent boundary layer (ZPGTBL). If we further assume that  $Re \gg Re_{\Delta}^{\text{min}}$ , the number of control volumes can be shown to scale as

$$N_{\text{points}} \sim N_{bl} Re (Re_{\Delta}^{\text{min}})^{-5/6}, \quad (3.5)$$

which is confirmed in Figures 3(c) and (d) using the data obtained using Eq. (3.4) for the NASA Juncture Flow.

The two isolines in Figure 3(a) bound the region  $N_{\text{points}} = 100$  million to 1000 million grid points, which are within the reach of current computing resources available to the industry. For example, for  $N_{bl} \approx 10$  and  $Re_{\Delta}^{\text{min}} \approx 10^4$ , the required number of points is  $\sim 400$  million, which can be currently simulated in a few days using thousands of cores. However, if the desired accuracy for the quantities of interest is such that  $N_{bl} \approx 20$  and  $Re_{\Delta}^{\text{min}} \approx 10^3$ , the number of grid points rises up to 3000 million, which renders WMLES unfeasible as a routine tool for the industry. Hence, the key to the success of WMLES as a designing tool resides in the accuracy of the solution achieved as a function of  $N_{bl}$  and  $Re_{\Delta}^{\text{min}}$ . This calls for a systematic error characterization of the quantities of interest, which is the objective of the present preliminary work.

#### 4. Error scaling of WMLES

The solutions provided by WMLES are grid-dependent and multiple computations are required in order to faithfully assess the quality of results. This raises the fundamental question of what is the expected WMLES error as a function of the flow parameters and grid resolution. Here, we follow the systematic error-scaling characterization from Lozano-Durán & Bae (2019). Taking the experimental values ( $q^{\text{exp}}$ ) as ground truth, the error in the quantity  $\langle q \rangle$  can be expressed as

$$\varepsilon_q \equiv \frac{\|\langle q^{\text{exp}} \rangle - \langle q \rangle\|_n}{\|\langle q^{\text{exp}} \rangle\|_n} = f\left(\frac{\Delta}{\delta}, Re, Ma, \text{geometry}, \dots\right), \quad (4.1)$$

where  $\|\cdot\|_n$  is the  $L_2$ -norm along the spatial coordinates of  $\langle q \rangle$ , and the error function can depend on additional non-dimensional parameters of the problem. For a given geometry and flow regime, the error function in Eq. (4.1) in conjunction with the cost map in Figure 3(a) determines whether WMLES is a viable approach in terms of accuracy and computational resources available. For the NASA Juncture Flow, the geometry,  $Re$ , and  $Ma$  are fixed parameters. If we further assume that the error follows a power law, Eq. (4.1) can be simplified as

$$\varepsilon_q = c_q (\Delta/\delta)^{\alpha_q}, \quad (4.2)$$

where  $c_q$  and  $\alpha_q$  are constants that depend on the modeling approach and flow region (i.e., laminar, fully turbulent, separation,...). For turbulent channel flows, Lozano-Durán & Bae (2019) showed that  $\alpha_q \approx 1$  and  $c_q$  is of the same order for various SGS models.

We focus on the error scaling of pointwise time-averaged velocity profiles and pressure coefficient, which are used as a proxy to measure the quality of the WMLES solution. From an engineering viewpoint, the lift and drag coefficients are the most pressing quantities of interest in aerodynamics applications. However, these are integrated quantities



which do not provide flow details and are susceptible to error cancellation. The granularity provided by pointwise time-averaged quantities allows us to detect modeling deficiencies and aids the development of new models. Unfortunately, the pointwise friction coefficient is not available from the experimental campaign, which hinders our ability to assess the performance of the wall models more thoroughly.

#### 4.1. WMLES Cases and flow uncertainties

We perform WMLES of the NASA Juncture Flow with a leading-edge horn at  $Re = 2.4 \times 10^6$  and  $AoA=5^\circ$ . Seven cases are considered. In the first six cases, we use grids generated using strategy (i) with constant grid size in millimeters akin to the example offered in Figure 1(a). In this case, the direct impact of  $Re_{\Delta}^{min}$  can be absorbed into  $\Delta/\delta$  as is done in Eq. (4.2). The grid sizes considered are  $\Delta \approx 6.7, 4.3, 2.2, 1.1$  and  $0.5$  millimeters, which are labeled as C-D7, C-D4, C-D2, C-D1, and C-D0.5, respectively. Cases C-D7, C-D4, and C-D2 are obtained by refining the grid across the entire aircraft surface. For cases C-D1 and C-D0.5, the grid size is, respectively, 1.1 and 0.5 millimeters only within a refinement box along the fuselage and wing-body juncture defined by  $x \in [1770, 2970]$  mm,  $y \in [-300, -200]$  mm, and  $z \in [-50, 150]$  mm. An additional case is considered to assess the impact on the accuracy of BL-conforming Voronoi grids. The grid is generated using strategy (ii) for  $N_{bl} = \delta/\Delta = 5$  and  $Re_{\Delta}^{min} = 8 \times 10^3$ , as shown in Figure 1(b). The case is denoted as C-N5-Rem8e3.

In the following,  $\langle \cdot \rangle$  and  $(\cdot)'$  denote time-average and fluctuating component, respectively. For comparison purposes, the profiles are interpolated to the grid locations of the experiments. Statistical uncertainties in WMLES quantities are estimated assuming uncorrelated and randomly distributed errors following a normal distribution. The uncertainty in  $\langle q \rangle$  is then estimated as  $\Delta \langle q \rangle \equiv \sigma/\sqrt{N_s}$ , where  $N_s$  is the number of samples for the computing  $\langle q \rangle$ , and  $\sigma$  is the standard deviation of the samples. The uncertainties for the mean velocity profiles and pressure coefficient were found to be below 1% and are not reported in the plots.

#### 4.2. Mean velocity profiles and Reynolds stresses

We consider three locations on the aircraft: (1) the upstream region of the fuselage, (2) the wing-body juncture, and (3) wing-body juncture close to the trailing edge. The mean velocity profiles are shown in panel (a) of Figures 4, 5, and 6 for each location considered and the errors are quantified in Figure 7(a). We assume that  $\langle u_i \rangle \approx \langle u_i^{\text{exp}} \rangle$  and the mean velocity from WMLES is directly comparable with unfiltered experimental data ( $\langle u_i^{\text{exp}} \rangle$ ). The approximation is reasonable for quantities dominated by large-scale contributions, as is the case for  $\langle u_i \rangle$ . Figure 4(a) shows that  $\langle u_i \rangle$  from WMLES converges to the experimental results with grid refinement. The turbulent boundary layer over the fuselage is about 10 to 20 mm thick, which yields roughly 3–6 points per boundary-layer thickness at the grid resolutions considered. Assuming that the flow at a given station can be approximated by a local canonical ZPGTBL, the expected error in the mean velocities can be estimated as  $\varepsilon_m \approx 0.16\Delta/\delta$  (Lozano-Durán & Bae 2019). For the current  $\Delta$ , this yields errors of 2%–8%, consistent with the results in Figure 7(a) (red symbols). The situation differs for the wing-body juncture and wing trailing edge. Despite the finer grid sizes, errors in the mean flow prediction are about 15% in the juncture (black symbols in Figure 7a) and even 100% in the trailing edge (blue symbols in Figure 7a). The larger errors may be attributed to the presence of a three-dimensional boundary layers and flow separation in the vicinity of the wing-body juncture and trailing

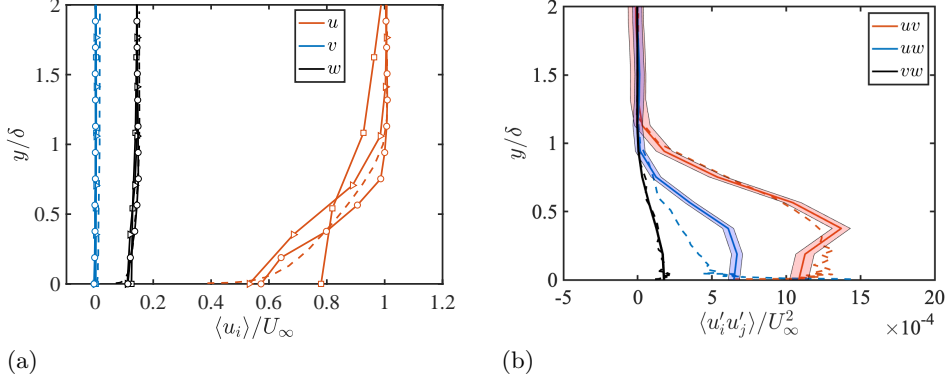


FIGURE 4. (a) Mean velocity profiles and (b) Reynolds stresses at location 1: upstream region of the fuselage  $x = 1168.4$  mm and  $z = 0$  mm (red line in Figure 7(b)). Solid lines with symbols denote WMLES for cases C-D7 ( $\square$ ), C-D4 ( $\triangleright$ ), and C-D2 ( $\circ$ ). Colors denote different velocity components. Panel (b) only includes case C-D2 and the shaded area represents statistical uncertainty. Experiments are denoted by dashed lines. The distance  $y$  is normalized by the local boundary-layer thickness  $\delta$  at that location.

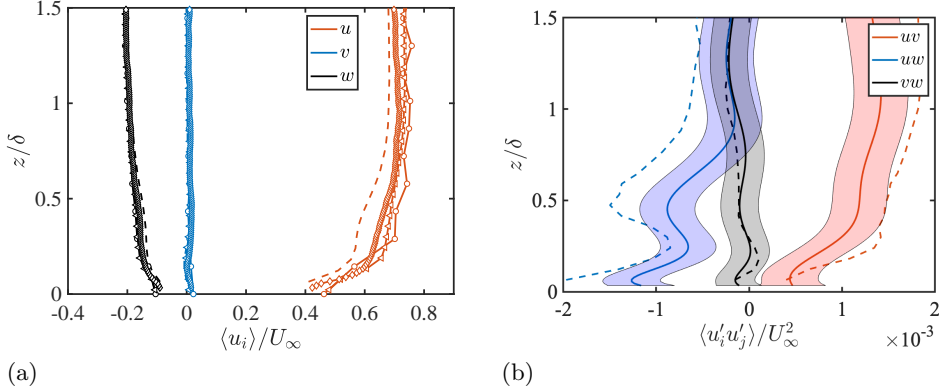


FIGURE 5. Same as Figure 4 for location 2: wing-body juncture at  $x = 2747.6$  mm and  $y = 239.1$  mm (black line in Figure 7(b)). In panel (a), lines with symbols are for cases C-D2 ( $\circ$ ), C-D1 ( $\triangleleft$ ), and C-D0.5 ( $\diamond$ ). In panel (b), the case shown in C-D0.5.

edge, which makes the error scaling predicated upon the assumption of local similarity to a ZPGTBL inappropriate.

The resolved portion of the tangential Reynolds stresses is shown in Figure panels (b) of Figures 4, 5, and 6. The trends followed by  $\langle u'_i u'_j \rangle$  are correctly captured at the different stations investigated, although their magnitudes tend to be systematically underpredicted, especially for the juncture region and trailing edge. Estimations from Lozano-Durán & Bae (2019) suggest that the error for the turbulence intensities should scale as  $\sim (\Delta/\delta)^{2/3}$ , which for the present grid resolution implies  $\sim 10$ – $20\%$  error. The result is consistent with the typical  $\Delta$  for WMLES, which supports a limited fraction of the turbulent fluctuations. Assuming  $\langle u_i^{\text{exp}} \rangle \approx \langle u_i \rangle$ , then  $\langle u_i^{\text{exp}} u_j^{\text{exp}} \rangle \approx \langle u_i u_j \rangle + \langle \tau_{ij}^{\text{SGS}} \rangle$ , where  $\tau_{ij}^{\text{SGS}}$  is the subgrid-scale tensor. Thus, for the current grid sizes we can expect

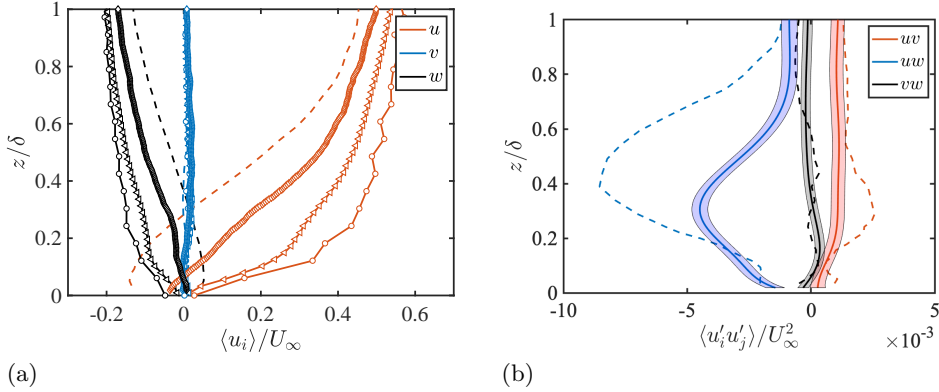


FIGURE 6. Same as Figure 4 for location 3: wing-body junction close to the trailing-edge at  $x = 2922.6$  mm and  $y = 239.1$  mm (blue line in Figure 7(b)). In panel (a), lines with symbols are for cases C-D2 ( $\circ$ ), C-D1 ( $\triangleleft$ ), and C-D0.5 ( $\diamond$ ). In panel (b), the case shown in C-D0.5.

$|\langle u'_i u'_j \rangle| < |\langle u'^{\text{exp}}_i u'^{\text{exp}}_j \rangle|$ , i.e., severe underprediction of the tangential Reynolds stress by WMLES.

Figure 7(a) is the cornerstone of the present study. It shows the relative errors in the prediction of the mean velocity profiles for the three regions considered: upstream fuselage, wing-body junction, and wing-body junction at the trailing edge. The three regions are marked with lines in Figure 7(b) using the same colors as in Figure 7(a). The turbulent flow in the fuselage resembles a ZPGTBL. As such, the wall- and SGS models, which have been devised for and validated in flat-plate turbulence, perform accordingly. On the contrary, there is a clear decline of current models in the wing-body junction and trailing edge region, which are dominated by secondary motions in the corner and flow separation. Not only is the magnitude of the errors larger in the latter locations, but the error rate of convergence is also slower ( $\varepsilon_m \sim (\Delta/\delta)^{0.5}$ ) when compared with the equilibrium conditions encountered in ZPGTBL ( $\varepsilon_m \sim (\Delta/\delta)$ ). The situation could be even more unfavorable, as Lozano-Durán & Bae (2019) has shown that for refining grid resolutions the convergence of WMLES towards the DNS solution may follow a non-monotonic behavior due to the interplay between numerical and SGS model errors.

#### 4.3. Pressure coefficient

The surface pressure coefficient over the wing,  $C_p$ , is shown in Figure 8 along the chord of the wing. The predictions are compared with experimental data at three different  $y$ -locations. The locations selected are denoted by red lines in Figure 8(d). Overall, WMLES agrees with the experimental data to within 1–5% error. The predictions are still to within 5% accuracy even at the coarsest grid resolutions considered, which barely resolved the boundary layer. The main discrepancies with experiments are located at the leading edge of the wing.

The accurate prediction of  $C_p$  is a common observation in CFD of external aerodynamics. The result can be attributed to the outer-layer nature of the mean pressure, which becomes less sensitive to the details of near-wall turbulence. Under the thin boundary-layer assumption, the integrated mean momentum equation in the spanwise direction shows that  $\langle p \rangle + \rho \langle v^2 \rangle \approx p_e(x) \Rightarrow p_{\text{wall}} = p_e(x)$ , where  $p_e$  is the far-field pressure. Hence, the pressure at the surface is mostly imposed by the inviscid imprint of the outer flow.

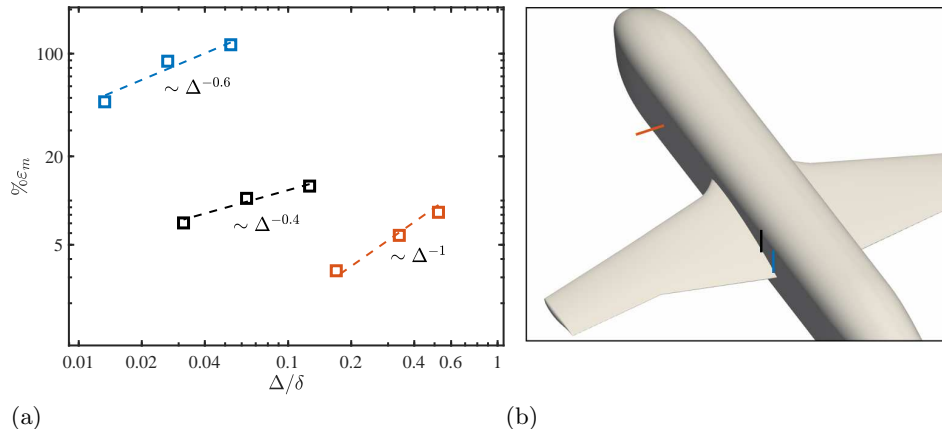


FIGURE 7. (a) Error in the mean velocity profile prediction by WMLES as a function of the grid resolution. The different colors denote the three locations indicated in panel (b) using the same color code.

This is demonstrated by performing an additional calculation similar to C-D2 but imposing the free-slip boundary condition at the wall such that boundary layers are unable to develop (Figure 8(c)). The conditions for  $p_{\text{wall}} = p_e(x)$  would not hold, for example, when the wall radius of curvature is comparable to the boundary-layer thickness. This is the case in the vicinity of the wing leading-edge, which is the region where the accuracy of  $C_p$  provided for WMLES is the poorest and most sensitive to  $\Delta$ . The tripping methodology used in WMLES differs from the experimental setup, which may also contribute to the discrepancies observed.

The outer-flow character of  $C_p$  is encouraging for the prediction of the pressure-induced components of the lift and drag coefficients. It also suggests that  $C_p$  might not be a challenging quantity to predict in the presence of wall-attached boundary layers. Thus, the community should focus the efforts on other important quantities of interest such as the numerical prediction of the skin-friction coefficient and its challenging experimental measurement.

#### 4.4. Separation bubble

For completeness, we also report the results on the size of the separation bubble. The mean wall-stress streamlines for case C-D0.5 are shown in Figure 9. The figure also contains a depiction of the average length and width of the separation bubble, which are about 100 mm and 60 mm, respectively, for case C-D0.5. Direct comparison of these dimensions with oil-film experimental results show that the current WMLES prediction is about 15% lower than the experimental measurements ( $120 \times 80$  mm), consistent with previous WMLES investigations (Lozano-Durán *et al.* 2020; Iyer & Malik 2020; Ghate *et al.* 2020). Nonetheless, note that the sizes of the separation zone from WMLES are obtained from the tangential wall-stress streamlines after the wall stress is averaged in time, whereas the experimental sizes are obtained from the pattern resulting from the oil-film time evolution. Albeit both methodologies provide an average description of the size of the separation zone, they do not allow for a one to one comparison and we should not interpret the present differences as a faithful quantification of the errors. Hence, a

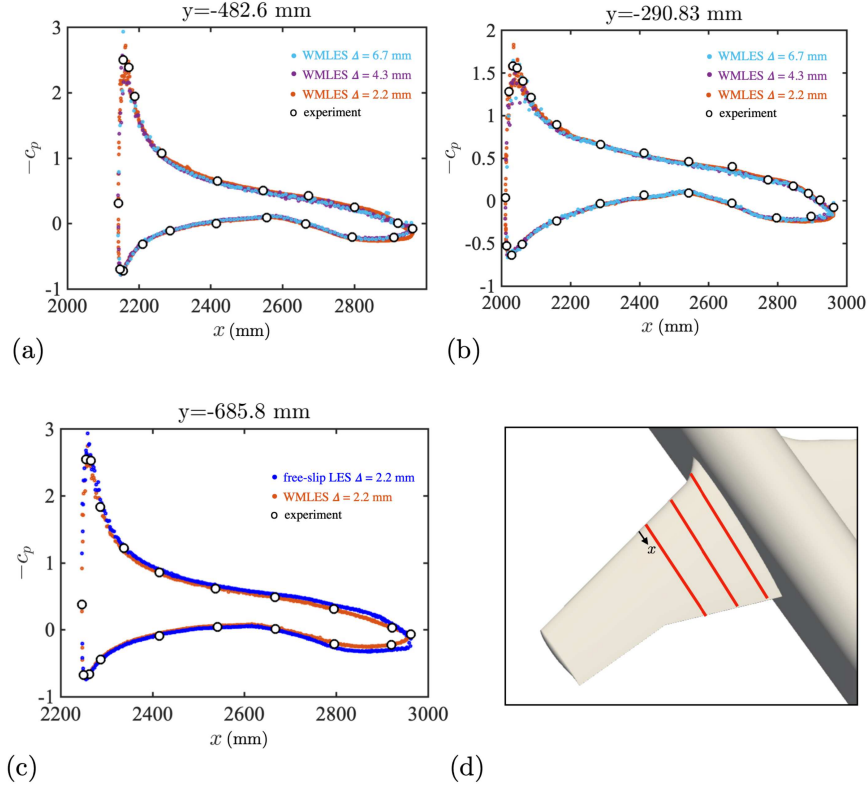


FIGURE 8. The surface pressure coefficient  $C_p$  along the wing. Panels (a) and (b) show  $C_p$  for cases C-D7, C-D4 and C-D2. Panel (c) shows  $C_p$  for case C-D2 and a case identical to C-D2 but imposing free-slip boundary condition at the walls. (d) Locations over the wing selected to represent  $C_p$  in panels (a), (b) and (c).

methodology allowing for quantitative comparisons of separated-flow patterns between CFD and experimental data remains an open challenge.

#### 4.5. Improvements with boundary-layer-conforming grids

We evaluate potential improvements with BL-conforming grids by comparing the results for case C-N5-Rem8e3 with case C-D2. The grid for C-N5-Rem8e3 is generated for  $N_{bl} = 5$  and  $Re_{\Delta}^{\min} = 10^4$  following the procedure described in Section 3.1. For reference, case C-D2 has 32 million control volumes, whereas case C-N5-Rem8e3 has 11 million control volumes. The mean velocity profiles for C-N5-Rem8e3 are shown in Figure 10 and compared with C-D2 at three locations. Some moderate improvements are achieved at the fuselage despite both cases sharing the same  $N_{bl}$  at that location. The improvements are accentuated at the juncture and trailing edge, where C-N5-Rem8e3 outperforms C-D2 with less than a fourth of the grid points per  $\delta$  in each of the three spatial directions.

The results suggest that grids designed to specifically target the boundary layer could improve the overall accuracy of WMLES. The outcome might be explained by considering the upstream history of the WMLES solution at a given station. Let's assume the simpler scenario of WMLES of a flat-plate turbulent boundary layer along  $x$  using two grids: a constant-size grid and a BL-conforming grid. If we take an  $x$ -location at which both grids have the same  $N_{bl}$ , the upstream flow for the constant-size grid is underresolved

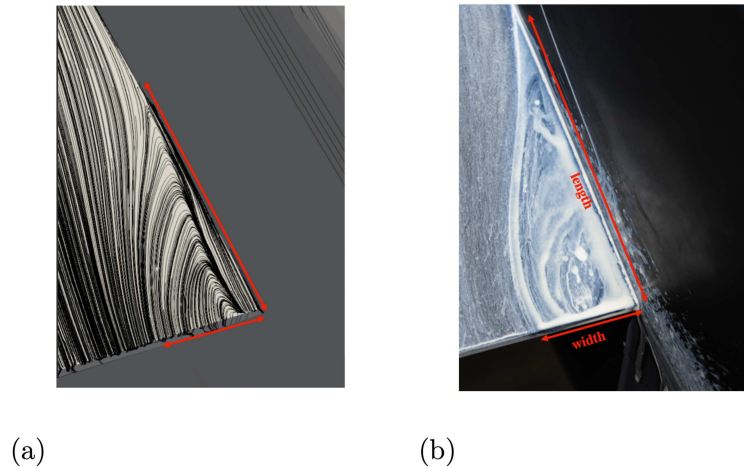


FIGURE 9. Streamlines of the average tangential wall-stress. The results are for case C-D0.5.

compared to the BL-conforming grid due to the thinner  $\delta$  upstream the flow (hence, less points per  $\delta$  and larger errors). On the other hand, the BL-conforming grid maintains a constant grid resolution scaled in  $\delta$  units and effectively more resolution upstream the flow. Furthermore, even if at a given  $x$  location  $N_{bl}$  is larger for the constant-size grid, the solution could be worse because of error propagation from the upstream flow. By assuming that energy-containing eddies with lifetimes  $\delta/U_\infty$  are advected by  $U_\infty$ , we can estimate the downstream propagation of errors at a given location  $x_0$  by  $\Delta x_e = \int_{x_0}^x \delta_0/\delta dx$ , which is the streamwise distance required for the energy-containing eddies to forget their past history. In ZPGTBL at high  $Re$  (Sillero *et al.* 2013),  $\Delta x_e$  can reach values of  $\Delta x_e \approx 100\delta_0$ . The long convective distance for error propagation ( $\sim 200$  mm for  $\delta_0 \approx \Delta = 2$  mm) combined with the higher upstream errors for constant-size grids may explain the improved results for C-N5-Rem8e3 reported in Figure 10.

## 5. Conclusions

We have performed WMLES of the NASA Juncture Flow using charLES with Voronoi grids. The simulations were conducted for an angle of attack of  $5^\circ$  and  $Re = 2.4 \times 10^6$ . We have characterized the errors in the prediction of mean velocity profiles and pressure coefficient for three different locations over the aircraft: the upstream region of the fuselage, the wing-body juncture, and the wing-body juncture close to the trailing-edge. The last two locations are characterized by strong mean-flow three-dimensionality and separation.

The prediction of the pressure coefficient is below 5% error for all grid sizes considered, even when boundary layers were marginally resolved. We have shown that this good accuracy can be attributed to the outer-layer nature of the mean pressure, which becomes less sensitive to flow details within the turbulent boundary layer. A summary of the errors

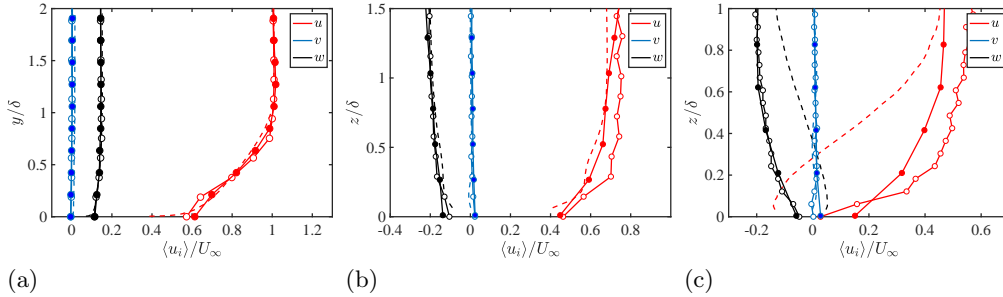


FIGURE 10. Mean velocity profiles for case C-N5-Rem8e3 (solid lines with  $\bullet$ ) and C-D2 (solid lines with  $\circ$ ) at (a) location 1: upstream region of the fuselage  $x = 1168.4$  mm and  $z = 0$  mm (b) location 2 wing-body juncture  $x = 2747.6$  mm and  $y = 239.1$  mm, and (c) location 3: wing-body juncture close to the trailing edge at  $x = 2922.6$  mm and  $y = 239.1$  mm. Experiments are denoted by dashed lines. Colors denote different velocity components. The distance  $y$  is normalized by the local boundary-layer thickness  $\delta$  at that location.

incurred by WMLES in predicting mean velocity profiles is shown in Figure 7 for the three locations considered. The message conveyed by the error analysis is that WMLES performs as expected in regions where the flow resembles a zero-pressure-gradient flat plate boundary layer. However, there is a clear decline of the current models in the presence of wing-body junctions and, more acutely, in separated zones. Moreover, the slow convergence to the solution in these regions renders the brute-force grid-refinement approach to improve the accuracy of the solution unfeasible. The results reported above pertain to the mean velocity profile predicted using the typical grid resolution for external aerodynamics applications, i.e., 5–20 points per boundary-layer thickness. The impact of the above deficiencies on the skin friction prediction is uncertain due to the lack of experimental measurements. Yet, it is expected that the errors observed in the mean velocity profile would propagate to the wall stress.

Finally, we have shown that boundary-layer-conforming grids (i.e., grids maintaining a constant number of points per boundary-layer thickness) allow for a more efficient distribution of grid points and smaller errors. It was argued that the improved accuracy might be due to the reduced propagation of WMLES errors in the streamwise direction. The increased accuracy provided by boundary-layer-conforming grids will be investigated in more detail in future studies along with the effect of targeted refinement in the wakes. Our results suggest that novel modeling venues encompassing physical insights, together with numerical and gridding advancements, must be exploited to attain predictions within the tolerance required for Certification by Analysis.

## Acknowledgments

A.L.-D. acknowledges the support of NASA under grant No. NNX15AU93A. We thank Jane Bae and Konrad Goc for helpful comments.

## REFERENCES

- BOSE, S. T. & PARK, G. I. 2018 Wall-modeled large-eddy simulation for complex turbulent flows. *Annu. Rev. Fluid Mech.* **50**, 535–561.

- CHAPMAN, D. R. 1979 Computational aerodynamics development and outlook. *AIAA J.* **17**, 1293–1313.
- CHOI, H. & MOIN, P. 2012 Grid-point requirements for large eddy simulation: Chapman’s estimates revisited. *Phys. Fluids* **24**, 011702.
- CLARK, A. M., SLOTNICK, J. P., TAYLOR, N. J. & RUMSEY, C. L. 2020 Requirements and challenges for CFD validation within the High-Lift Common Research Model ecosystem. *AIAA Paper* 2020-2772.
- GERMANO, M., PIOMELLI, U., MOIN, P. & CABOT, W. H. 1991 A dynamic subgrid-scale eddy viscosity model. *Phys. Fluids* **3**, 1760.
- GHATE, A. S., HOUSMAN, J. A., STICH, G.-D., KENWAY, G. & KIRIS, C. C. 2020 Scale Resolving Simulations of the NASA Juncture Flow Model using the LAVA Solver. *AIAA Paper* 2020-2735.
- IYER, P. S. & MALIK, M. R. 2020 Wall-modeled LES of the NASA Juncture Flow Experiment. *AIAA Paper* 2020-1307.
- KAWAI, S. & LARSSON, J. 2012 Wall-modeling in large eddy simulation: Length scales, grid resolution, and accuracy. *Phys. Fluids* **24**, 015105.
- KEGERISE, M. A., NEUHART, D., HANNON, J. & RUMSEY, C. L. 2019 An experimental investigation of a wing-fuselage junction model in the NASA Langley 14- by 22-foot subsonic wind tunnel. *AIAA Paper* 2019-0077.
- LARSSON, J., KAWAI, S., BODART, J. & BERMEJO-MORENO, I. 2016 Large eddy simulation with modeled wall-stress: recent progress and future directions. *Mech. Eng. Rev.* **3**, 1–23.
- LEE, H., PULLIAM, T., RUMSEY, C. & CARLSON, J.-R. 2018 Simulations of the NASA Langley 14-by 22-Foot Subsonic Tunnel for the Juncture Flow Experiment. In *NATO STO*.
- LEE, H. C. & PULLIAM, T. H. 2019 Overflow juncture flow computations compared with experimental data. *AIAA Paper* 2019-0080.
- LEE, H. C., PULLIAM, T. H., NEUHART, D. & KEGERISE, M. A. 2017 CFD analysis in advance of the NASA Juncture Flow Experiment. *AIAA Paper* 2017-4127.
- LILLY, D. K. 1992 A proposed modification of the Germano subgrid-scale closure method. *Phys. Fluids* **4**, 633–635.
- LOZANO-DURÁN, A. & BAE, H. J. 2019 Error scaling of large-eddy simulation in the outer region of wall-bounded turbulence. *J. Comput. Phys.* **392**, 532–555.
- LOZANO-DURÁN, A. & BAE, H. J. 2020 Self-critical machine-learning wall-modeled LES for external aerodynamics. *Center for Turbulence Research - Annual Research Briefs* pp. XX–XX.
- LOZANO-DURÁN, A., BOSE, S. T. & MOIN, P. 2020 Prediction of trailing edge separation on the NASA Juncture Flow using wall-modeled LES. *AIAA Paper* 2020-1776.
- POINSOT, T. & LELE, S. 1992 Boundary conditions for direct simulations of compressible viscous flows. *J. Comput. Phys.* **101**, 104–129.
- RUMSEY, C. L. 2018 The NASA Juncture Flow Test as a model for effective CFD/experimental collaboration. *AIAA Paper* 2018-3319.
- RUMSEY, C. L., CARLSON, J. & AHMAD, N. 2019 FUN3D Juncture Flow computations compared with experimental data. *AIAA Paper* 2019-0079.
- RUMSEY, C. L. & MORRISON, J. H. 2016 Goals and status of the NASA Juncture Flow Experiment. In *NATO STO*.
- RUMSEY, C. L., NEUHART, D. & KEGERISE, M. A. 2016 The NASA Juncture Flow



- Experiment: goals, progress, and preliminary testing (Invited). *AIAA Paper* 2016-1557.
- SILLERO, J. A., JIMÉNEZ, J. & MOSER, R. D. 2013 One-point statistics for turbulent wall-bounded flows at Reynolds numbers up to  $\delta^+ \approx 2000$ . *Phys. Fluids* **25**, 105102.
- SLOTNICK, J., KHODADOUST, A., ALONSO, J., DARMOFAL, D., GROPP, W., LURIE, E. & MAVRIPLIS, D. 2014 *CFD Vision 2030 Study: A Path to Revolutionary Computational Aerosciences*.
- SPALART, P. R. 2009 Detached-eddy simulation. *Annu. Rev. Fluid Mech.* **41**, 181–202.
- SPALART, P. R., JOU, W. H., STRELETS, M., ALLMARAS, S. R. *et al.* 1997 Comments on the feasibility of LES for wings, and on a hybrid RANS/LES approach. *Advances in DNS/LES*, 4–8.
- VASSBERG, J. C., TINOCO, E. N., MANI, M., BRODERSEN, O. P., EISFELD, B., WAHLS, R. A., MORRISON, J. H., ZICKUHR, T., LAFLIN, K. R. & MAVRIPLIS, D. J. 2008 Abridged summary of the third AIAA computational fluid dynamics drag prediction workshop. *J. Aircr.* **45**, 781–798.
- WANG, M. & MOIN, P. 2002 Dynamic wall modeling for large-eddy simulation of complex turbulent flows. *Phys. Fluids* **14**, 2043–2051.